Nanoscale

Accepted Manuscript

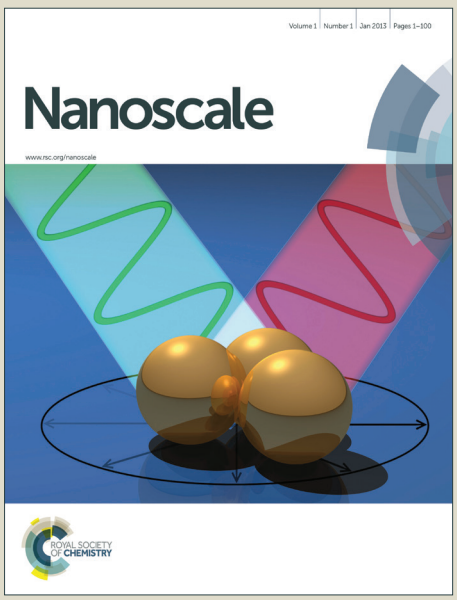

ROYAL SOCIETY OF CHEMISTRY

www.rsc.org/nanoscale

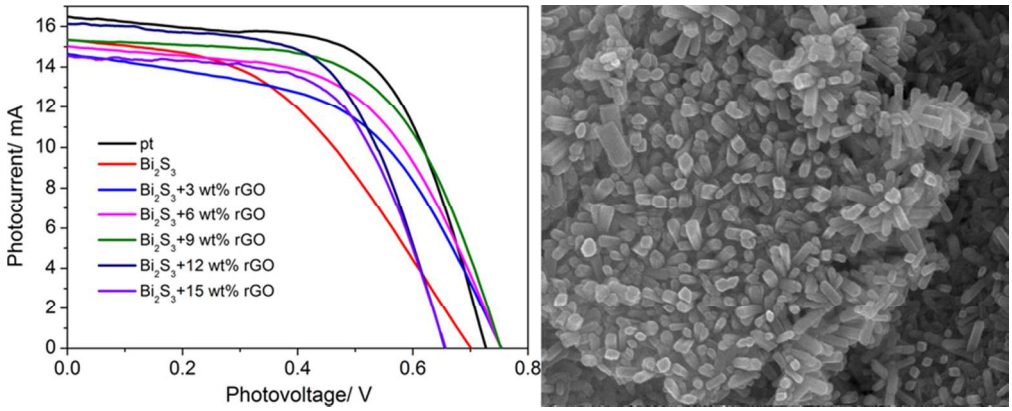

Graphical Abstract

80x32mm (300 x 300 DPI)

Mesoporous Bi_2S_3 Nanorods with Graphene-Assistance as Low-Cost Counter-Electrode Materials in Dye-Sensitized Solar Cells

Sheng-qi Guo,[a] Tian-zeng Jing,[a] Xiao Zhang,[a] Xiao-bing Yang,[c] Zhi-hao Yuan [*b] and Fang-zhong Hu [*c]

[a] Tianjin Key Laboratory of Environmental Remediation and Pollution Control, Nankai University, Tianjin 300071, China.

[b] Tianjin Key Lab for Photoelectric Materials & Devices, Tianjin 300384, China. E-mail: zhyuan@tjut.edu.cn

[c] State Key Laboratory and Institute of Elemento-Organic Chemistry, Nankai University, Tianjin 300071, China. E-mail: fzhu@nankai.edu.cn

In this work, we report the synthesis of mesoporous Bi_2S_3 nanorods under hydrothermal conditions without any additives, and investigated its catalytic activities as the CE in DSCs through I–V curves and tested conversion efficiency. To further improve their power conversion efficiency, we added different amounts of reduced graphene by simple physical mixing. With the help of 9 wt% amount of reduced graphene (rGO), its short-circuit current density, open-circuit voltage, fill factor were J_{sc}= 15.33 mA cm^{-2}, V_{oc}= 0.74 V and *FF*= 0.609. More importantly, its conversion efficiency reached 6.91%, which is slightly inferior to the commercial Pt counter electrode (7.44%). Compared with conventional Pt counter electrodes of solar cells, this new material has the advantages of low-cost, facile synthesis and high efficiency with graphene assistance. As far as we know, this Bi_2S_3 + 9 wt% rGO system has the best performance ever recorded in the all Bi_2S_3-based CEs in DSCs system.

Introduction

In the past two decades considerable scientific and industrial attention has been focused on dye-sensitized solar cells (DSCs) due to the simple fabrication procedures, environmental friendliness, transparency, and good plasticity.[1,2] The counter electrode (CE) is a crucial component of DSCs. Pt deposited on fluorine-doped tin oxide (FTO) conductive glass is a conventional and effective CE with good electrocatalytic properties for the reduction of triiodide to iodide.[3,4] However, due to its limited availability and costliness, finding alternatives for Pt in the DSCs system is crucial.[5] In recent studies, some inorganic materials have shown excellent electrocatalytic activity in reducing triiodide, which will possess important candidacy as promising alternative CE materials in DSCs.[6-9] In particular, carbon materials have been trying as CE because of their low cost and excellent corrosion resistance against the redox couple.[10,11]

Bismuth sulde (Bi_2S_3), as an important V–VI semiconductor material, exhibits a lamellar binary structure and crystallizes in the orthorhombic system (Pbnm space group).[12,13] Recent works on Bi_2S_3 revealed that they have great potential in memristor,[14] electrochemical[15] and optoelectronics.[16] Especially, Bi_2S_3 shows superior effect in DSCs as CE material, due to its low direct band gap of 1.2 – 1.7 eV, an absorption coefficient on the order of 10^4 -10^5 cm^{-1} and an incident photon to electron conversion efficiency of ~5%.[17] Shortly before, our group compared the catalytic activities of different facets within Bi_2S_3 *via* density functional theory (DFT) computation.[18] We found that the (130) facet has the largest surface energy, the best electrical conductivity and the highest position of the conduction band minimum, suggesting the highest catalytic activities of Bi_2S_3 with (130) facet and the most effective electron transfer from CE to triiodide. This conclusion was verified by experiments and the DSCs with (130)-facet Bi_2S_3 CE exhibited conversion efficiency of only 3.5%, which is rather higher than other Bi_2S_3 CEs such as (221)-faceted (1.9%). This shows that although Bi_2S_3 has these advantageous characteristics, the

result of the practical application in DSCs is not satisfactory. It is therefore urgent to find a method to improve the performance of Bi_2S_3 in DSCs.

For a long time, the combination of nanomaterials with graphene is considered as an effective way to improve electrochemical stability and conductivity.[19,20] It is because of graphene have various attractive properties such as high electrical conductivity, high Fermi velocity, linear energy dispersion relation and structural flexibility, which make it an ideal auxiliary for mixing or anchoring of insulating materials.[21-23] Inspired by these features, Bi_2S_3-graphene composites have been naturally explored and exhibit superior electrochemical performances for DSCs. Very recently, Chen group synthesized 3D Bi_2S_3 microspheres comprised of nanorods on graphene, and investigated its conversion efficiency tests as the CE in DSCs (5.5%).[16] To the best of our knowledge, this is the best reported performance among all Bi_2S_3 based CEs. Since graphene as substrate for Bi_2S_3 got success in DSCs, what will happen when combining two kinds of materials by simple physical mixing? It is very interesting to explore Bi_2S_3 with graphene assist as a safe CE for high conversion efficiency in dye-sensitized solar cells.

Herein, we report the synthesis of mesoporous Bi_2S_3 nanorods under hydrothermal conditions without any additives. The reaction parameters have been optimized. In the present work, we first investigated the photovoltaic properties of the Bi_2S_3 products mixing with graphene among different amount. The results show that mesoporous Bi_2S_3 nanorods with appropriate amount of graphene assist can be a low-cost substitution for Pt CEs.

Experimental section

Synthesis of mesoporous Bi_2S_3 nanorods

All reagents are of analytic grade and used without further purification. In the typical synthesis procedure, 1g $Bi(NO_3)_3$ was put into 25mL of deionized water under stirring to form a homogenous solution. Subsequently, 0.8g thioacetamide was added in under stirring. A brown colloid suspension was formed instantly. And then the precursor mixture was transferred into a Teflon-lined stainless steel autoclave and heated at 120 ℃ for 24 h. After the sample was gradually cooled to room temperature, a black precipitate was collected and then washed with distilled water and absolute ethanol, and the sample was kept in absolute ethanol.

Preparation of Graphene oxide (GO) Nanosheets

All the reagents are of analytic grade and were used without any purification. Graphene oxide (GO) nanosheets were prepared by a modified Hummers method. In detail, graphite powder (2.0 g) was dispersed into 100 ml cooled (0 ℃) H_2SO_4 (98%), followed by slow addition of $KMnO_4$ (6.0 g). Then, the suspension was stirred at 35 ℃ for 3 days. Afterwards, 200 ml distilled water was added and kept at 98 ℃ for 2 h. When cooled to 60 ℃, 10 ml H_2O_2 (30%) was injected into the suspension to completely react with the excess KMnO4, and a bright yellow mixture was obtained. The suspension was centrifuged and washed with HCl (30%) and distilled water until the pH value was ~7. The precipitate was collected and stored for further use.

Characterization

X-ray diffraction analysis of the samples were carried out by an X-ray diffractometer (XRD, Rigaka D/max2500) with Cu Kα radiation (λ = 1.54056 Å). The morphology of the as-prepared products was characterized by scanning electron microscopy (SEM, Nova Nano SEM 230, FEI.) and transmission electron microscopy (TEM, Tecnai G^2F20, FEI). The elemental composition was detected by X-ray photoelectron spectroscopy (XPS, Kratos Axis Ultra DLD). The Brunauer−Emmett−Teller (BET) specific surface area (SBET) of the sample was analyzed by

nitrogen adsorption in a Tristar 3000 nitrogen adsorption apparatus, and AFM (Multimode8, Bruker). Cyclic voltammetry (CV) was implemented on an electrochemical workstation (ZAHNER ZENNIUM CIMPS-1, Germany) with a three-electrode system (the prepared CEs as the working electrode, a symmetrical platinum sheets as the counter electrode, and saturated calomel electrode as the pesudoreference electrode) in an anhydrous acetonitrile solution of 0.1 M $LiClO_4$, 10 mM LiI, and 1 mM I_2 at a scan rate of 50 mV S^{-1}. Electrochemical impedance spectroscopy (EIS) were executed on dummy cells with a typical symmetric sandwich-like structure, that is ,CE/electrolyte/CE, using an impedance measurement unit of workstation in the frequency range 0.1-10^6 Hz with an ac amplitude of 10 mV. The photocurrent density-voltage (*J*-V) measurements were carried out on a Keithley 2410 digital source meter under AM 1.5 illumination (continuous solar simulator for PV cells, 100 mW cm^{-2}), which was calibrated by a Si reference cell beforehand. All the measurements were executed at room temperature. The UV spectra were recorded on a Cary 5000 spectrometer at room temperature.

Photovoltaic Performance Tests.

Approximately 0.05 g of Bi_2S_3 powder was mixed with 0.5 mL of 2.5% PEG20000 solution and stirred until a fluid mixture formed. A film was then made using the doctor-blade method on FTO conductive glass (LOF, TEC-15, 15Wper square). The film was heated at 450 ℃ for 1 h under the protection of argon to obtain the Bi_2S_3 counter electrode. A commercial TiO_2 sol (Solaronix, Ti-Nanoxide T/SP) was used to prepare the TiO_2 film on FTO also through the doctor-blade method, and the film was soaked in an N-719 dye solution (in ethanol) for 24 h to obtain dye-sensitized TiO_2 electrodes. DSCs were assembled by injecting the electrolyte into the aperture between the dye-sensitized TiO_2 electrode and the counter electrode. The liquid electrolyte composed of 0.05 M I_2, 0.1M LiI, 0.6 M 1,2-dimethyl-3-propylimidazolium iodide (DMPII), and 0.5 M 4-tert-butyl pyridine with acetonitrile as the solvent. Surlyn 1702 was used as the spacer between the two electrodes. The two electrodes were clipped together and solid paraffin was used as the sealant to prevent the electrolyte solution from leaking. The effective cell area was 0.25 cm^2.

Results and discussion

The phase and structures of the as-synthesized samples were determined by X-ray powder diffraction (XRD) analysis. Figure 1 shows the XRD pattern of the as-synthesized Bi_2S_3. It can be seen that the XRD pattern conforms to the orthorhombic Bi_2S_3 in space group Pbnm (a= 11.15 Å, b= 11.30 Å, c= 3.98 Å, JCPDS: 17-0320), and the intense and sharp peaks indicate that the product is well crystallized. From Figure 1, it can also be seen that the (211) plane was unusual stronger than the corresponding conventional values. This means that the resultant Bi_2S_3 products were mainly dominated by the (211) plane. Therefore, the (211) plane was preferentially oriented parallel to the surface of the supporting substrate in the experiment. Further evidence for the composition was obtained by the EDS. Fig. S1 shows the typical EDS spectra of the as-synthesized Bi_2S_3 sample. The ratio of Bi to S is approximately 1: 1.53, which reveals that the sample has high purity.

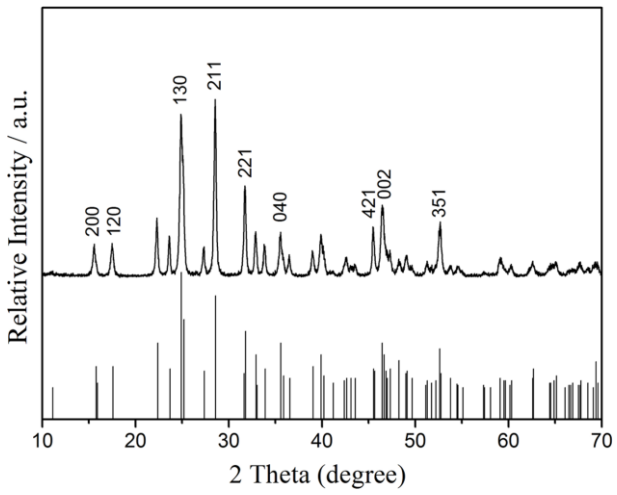

Figure 1. XRD pattern of the synthetic Bi_2S_3 nanorods.

The morphology of the as-synthesized Bi_2S_3 was studied by scanning electron microscopy (SEM) and transmission electron microscopy (TEM). As shown in Figure 2a and 2b, the typical morphology of the as-prepared Bi_2S_3 is nanorod structure with the length ranging from 50 to 90 nm. Figure 2c and 2e show typical TEM images of several Bi_2S_3 nanorods. Similar to the SEM images, these nanorods have length below 100 nm. The high-resolution TEM image (Fig. 2d)

shows that the crystalline lattice distances in the white frame are 3.12 Å and 2.81 Å, corresponding to the (211) and (221) planes of orthorhombic Bi_2S_3, respectively, which are consistent with the XRD results. As for porosity, the N_2 physisorption measurements isotherms for Bi_2S_3 nanorods is characteristic of a typical type III isotherm based on Brunauer-Deming-Deming-Teller (BDDT) classification (Fig. 3). The BET surface area reaches 11.80 m^2g^{-1}, and the average pore size was calculated as ~25 nm, which is the characteristic isotherm of mesoporous materials. The mesoporous structure can be seen clearly in higher magnification images in Figure 2f.

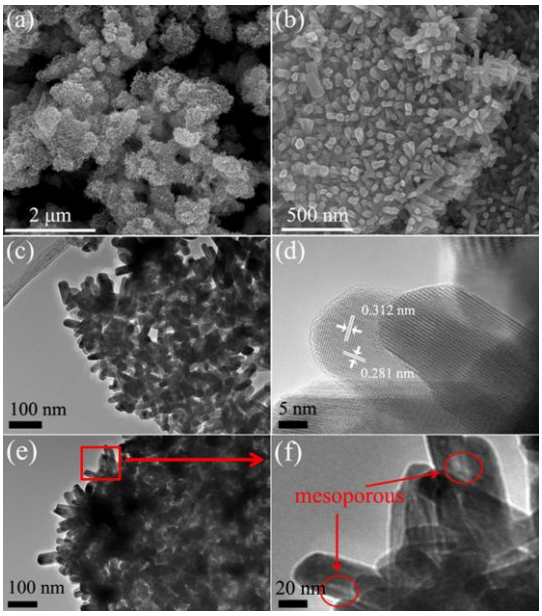

Figure 2. SEM images of the Bi_2S_3 nanorods: a) low magnification, b) high magnification. TEM images of the Bi_2S_3 nanorods: c, e and f) low magnification, d) HRTEM image."

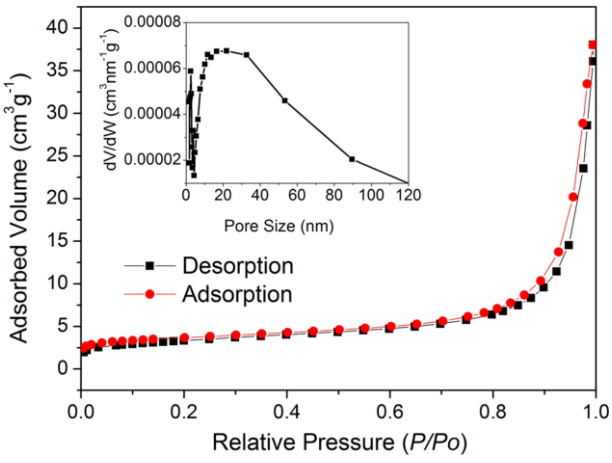

Figure 3. N_2 adsorption/desorption isotherm and Barrett-Joyner-Halenda (BJH) pore size distribution plot (inset) of Bi_2S_3 nanorods.

The relationship between the morphology of the mesoporous Bi_2S_3 nanorods and synthesis time was investigated. We conducted time-dependent experiments with different synthetic times from 1 to 24 h. XRD patterns in Figure 4d is clearly illustrated that the Bi_2S_3 phase will form pretty fast, after reacting for just 1 h. However, there is no regular morphology was found at initial (Fig. 4a). At 2 h, particles sizes varying around tens of nanometers with agglomeration were obtained (Fig. 4b). As the reaction time was increased to 8 h, large numbers of nanorods were produced but there exists some nanosheets and irregular shape product as observed (Fig. 4c). As the reaction proceeds to 24 h, regular and uniform nanorods have been formed (Fig. 2a). The results reveal that reaction time is one of the main factors in forming nanorod Bi_2S_3.

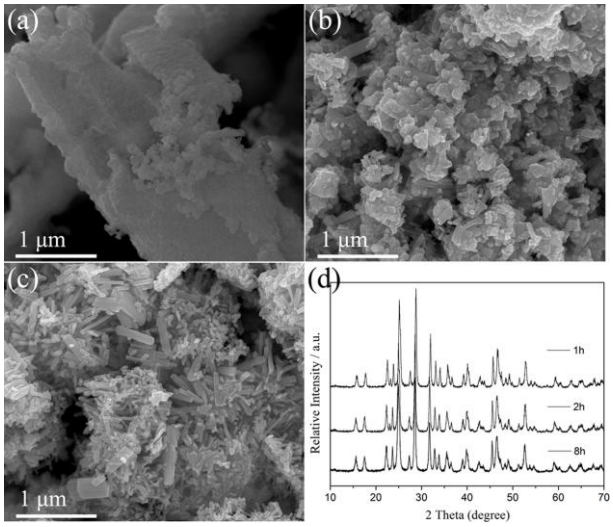

Figure 4. SEM images of the samples synthesized at 120 ℃ for a) 1 h, b) 2 h, c) 8 h, and d) XRD patterns of the as-prepared Bi_2S_3 products.

The samples were tested as counter electrode materials in dye-sensitized solar cells. When as-prepared Bi_2S_3/FTO film was used as CE, the photovoltaic characteristics were V_{oc} = 0.696V, J_{sc} = 15.34 mA cm^{-2}, FF = 0.447, and η = 4.78% (its SEM image, N_2 adsorption/desorption isotherm and Barrett-Joyner-Halenda (BJH) pore size shown in Figure S2 and S3 in the Supporting Information after calcined at 450 ℃, respectively). We found that as-prepared Bi_2S_3 exhibit high

power conversion efficiency. It can be attributed to their mesoporous structural features. Figure S3 shows that the as-prepared Bi_2S_3 still possess mesoporous structure after calcined at 450 ℃, mesoporous structure causes the light waves to penetrate deep inside the catalyst and beget high mobility of charge, which is obviously beneficial for the enhancement of catalytic activity and power conversion efficiency.[24-26]

As mentioned above, due to graphene has some specific properties such as high electrical conductivity, we tried to mix in a few reduced graphene oxide (rGO) in order to enhance the power conversion efficiency (AFM images and XRD pattern of rGO shown in Figure S4 and S5 in the Supporting Information, respectively). Figure 5 shows the photocurrent–voltage curves of five DSCs using as-prepared Bi_2S_3, Bi_2S_3+ 3 wt% rGO, Bi_2S_3+ 6 wt% rGO, Bi_2S_3+ 9 wt% rGO, Bi_2S_3+ 12 wt% rGO, Bi_2S_3+ 15 wt% rGO and Pt electrodes as CEs. As expected, with the addition of rGO of 3, 6, 9, 12 and 15 wt%, respectively, the CE performances have been improved substantially. Especially, the devices equipped with Bi_2S_3+ 9 wt% rGO CE yield energy conversion efficiencies (η) of 6.91%, which is slightly inferior to the Pt CE (7.44%). Therefore, the high catalytic activity of Bi_2S_3 with graphene assist is validated. The photovoltaic and electrochemical performance parameters for different CEs are summarized in Table 1.

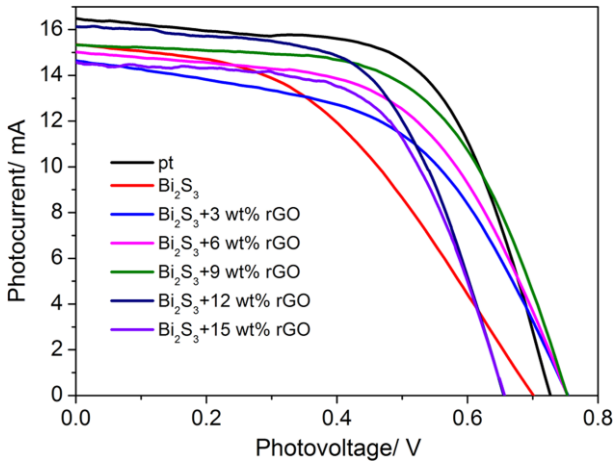

Figure 5. Photocurrent–voltage curves of DSCs with six Bi_2S_3-based CEs and Pt.

Table 1. Photovoltaic parameters[a] of the DSCs using nine kinds of CEs and a Pt CE and EIS parameters[b] of the dummy cells based on these electrodes

CEs	V_{oc}/(V)	J_{sc}/(mA cm^{-2})	*FF*	η(%)	R_s(Ω)	R_{ct}(Ω)	*CPE*	W_o(Ω)
Pt	0.73	16.47	0.618	7.44	4.04	1.70	0.91	0.36
Bi_2S_3	0.69	15.34	0.438	4.78	2.82	56.59	0.92	7.58
Bi_2S_3+3 wt%rGO	0.74	14.64	0.527	5.71	5.95	18.5	0.77	5.31
Bi_2S_3+6 wt%rGO	0.74	15.01	0.565	6.27	6.74	6.47	0.73	4.49
Bi_2S_3+9 wt%rGO	0.74	15.33	0.609	6.91	5.35	4.98	0.64	2.02
Bi_2S_3+12wt%rGO	0.65	16.02	0.608	6.27	6.78	6.21	0.68	2.95
Bi_2S_3+15wt%rGO	0.65	14.76	0.608	5.79	6.69	9.26	0.77	4.69

[a] V_{oc}: open-circuit voltage, J_{sc}: short-circuit current density, *FF*: fill factor, η: energy conversion efficiency. [b] R_s: series resistance, R_{ct}: charge transfer resistance in the CE/electrolyte interface, *CPE*: chemical capacitance in the CE/electrolyte interface, W_o: Warburg impedance. To make scientific comparative research on the performance of the seven CEs. Each kind of CE was made at the same conditions.

Due to the added carbon materials, the Bi_2S_3 catalytic properties were improved, it may attribute to the enhanced triiodide reduction or better contact between the electrolyte and the Bi_2S_3 catalyst as CoS.[27-29] Herein, to clearly evaluate the electrochemical catalytic activities of the six Bi_2S_3-based CEs to reduce triiodide, cyclic voltammetry (CV) were carried out in a three-electrode system at a scan rate of 50 mv s^{-1}. For comparison, we also measured the cyclic voltammograms of the Pt electrode under the same conditions. As shown in Figure 6, two typical pairs of reversible redox peaks were observed for both Pt electrodes. The pair of peaks at low potential can be attributed to the redox reaction of eqn (1), whereas the pair at high potential can be attributed to the redox reaction of eqn (2).[30]

$$I_3^- + 2e \leftrightarrow 3I^- \quad (1)$$

$$3I_2 + 2e \leftrightarrow 2I_3^- \quad (2)$$

The CV curves of iodide/ triiodide redox species using six kinds of Bi_2S_3-based materials were shown in Figure 7, Bi_2S_3 and Bi_2S_3+ 15 wt% rGO electrodes exhibit one pair of redox peak assigned to the reaction eqn (1). Compared with other five Bi_2S_3-based electrodes, the profile and peak location of the CV for the Bi_2S_3+ 9 wt% rGO electrode is more similar to that of Pt,

demonstrating the similar electrochemical catalytic activity. Besides, both Bi_2S_3+ 6 wt% rGO and Bi_2S_3+ 9 wt% rGO electrodes exhibit large current density indicating faster charge transfer process, which lead to high electrochemical catalytic activity.[31]

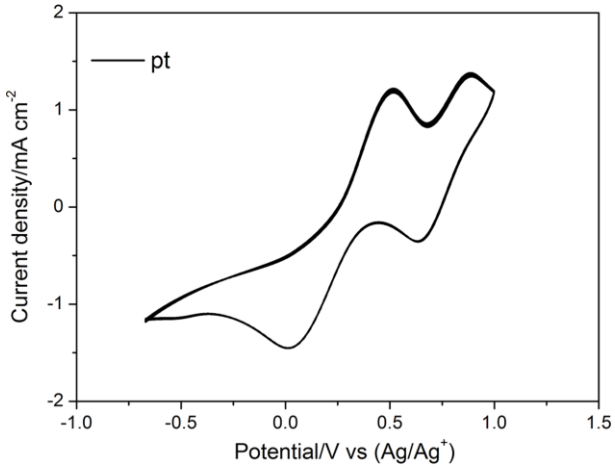

Figure 6. Cyclic voltammograms of the triiodide/iodide redox couple for Pt.

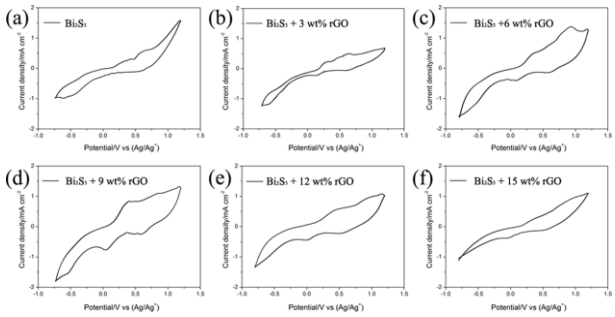

Figure 7. Cyclic voltammograms of the triiodide/iodide redox couple for six Bi_2S_3-based CEs.

Electrochemical impedance spectroscopy (EIS) was used to investigate the charge transfer process and the catalytic activity of a catalyst. The Nyquist plots of the symmetrical cells using various CEs are shown in Figure 8a, where two semicircles were observed among all Bi_2S_3-based CEs. The high-frequency (around 100 MHz) intercept on the real axis represents the series resistance (R_s). The semicircles maxima in the middle-frequency region represents charge-transfer resistance (R_{ct}) and the capacitance corresponding constant phase angle element (CPE) at the CE/electrolyte interface, while those in the low-frequency region offer information on the resistance at the finite layer Nernst diffusion impedance within the electrolyte. Figure 8b showed the equivalent circuit consists of several components. Herein, the R_{ct} value is calculated by fitting

the left-hand hump, and it varies inversely with the electrocatalytic activity for the reduction of triiodide, which is the key step of the catalytic process.[32,33] In table 1, Bi_2S_3+ 9 wt% rGO CE show larger R_{ct} (4.98 Ω) compared with other five Bi_2S_3-based CEs, which demonstrates the excellent catalytic activity of Bi_2S_3+ 9 wt% rGO CE, and explain the energy conversion efficiency of Bi_2S_3+ 9 wt% rGO CE slightly inferior to the Pt CE (1.70 Ω). W_o is the warburg impedance, which arises from mass-transport limitations due to the diffusion of the triiodide/iodide couple within the electrolyte. In addition, the W_o values of all Bi_2S_3-based CEs are much larger than that of Pt CE, illustrating the large diffusion impedance.[34] In addition, larger W_o and R_s values leads to relatively lower fill factor (*FF*).[35] Overall speaking, the EIS results agree with the photocurrent–voltage experiments.

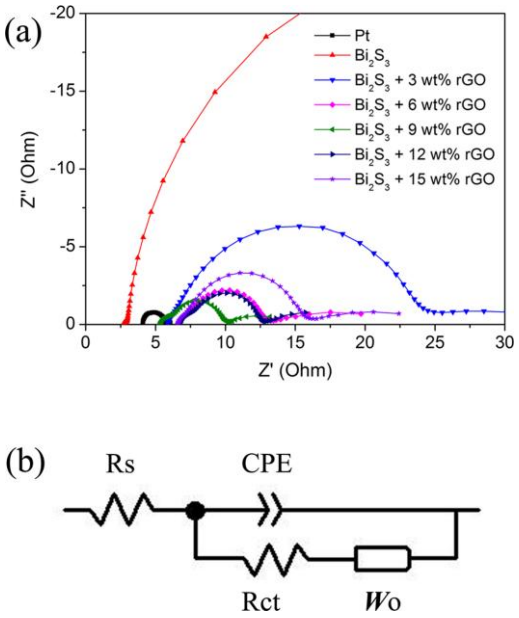

Figure 8. a) Nyquist plots of the symmetrical cells fabricated with Pt and six Bi_2S_3-based CEs; b) equivalent circuit diagram of the symmetrical cell.

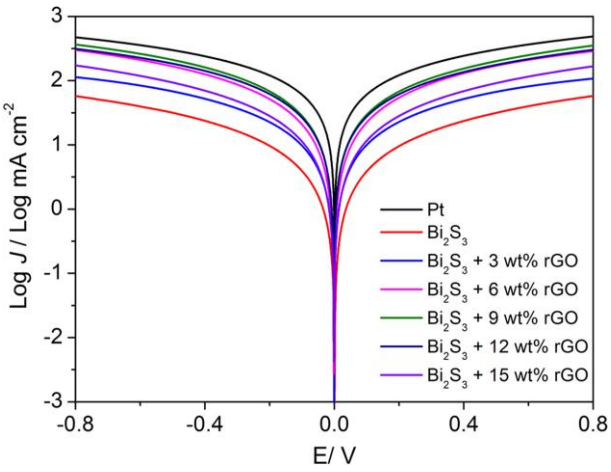

Figure 9. Tafel-polarization curves of different dummy cells that are the same as those used for EIS measurements.

Furthermore, Tafel-polarization measurements were conducted with the dummy cells used in EIS experiments. Figure 9 shows the logarithmic current density (log*J*) as a function of the voltage (*U*) for the oxidation/reduction of triiodide to iodide. According to the literature, at a low sweep rate, the limiting diffusion current density (J_{lim}) depends on the diffusion coefficient of the triiodide species in the electrolyte.[36] Herein, we found that except for pure Bi_2S_3 electrode, the J_{lim} values of the other six electrodes are of the analogous magnitude according to eqn (3). This means that there is a slight difference of diffusion coefficients among these electrodes. Where *D* is the diffusion coefficient of the triiodide, *l* is the spacer thickness, *n* is the number of electrons involved in the reduction of triiodide at the electrode, *F* is the Faraday constant and *C* is the triiodide concentration.[37]

(3)

In addition, the slopes for the anodic and cathodic branches are in the order of Pt > Bi_2S_3+ 9 wt% rGO > Bi_2S_3+ 12 wt% rGO > Bi_2S_3+ 6 wt% rGO > Bi_2S_3+ 15 wt% rGO > Bi_2S_3+ 3 wt% rGO > Bi_2S_3. The exchange current density (J_0) of the Bi_2S_3+ 9 wt% rGO was slightly inferior that of Pt, demonstrating that Bi_2S_3+ 9 wt% rGO had a relatively lower catalytic activity than Pt.[38] This results is in good agreement with the EIS parameters in terms of equ (4), where *R* is the gas

constant, *T* is the temperature, *Rct* is extracted from the electrochemical impendence spectra, *n* is the total number of individuals and *F* is the Faraday constant.[39]

(4)

The EIS and Tafel-polarization measurements have revealed that rGO plays the role of a binder and improves the bonding of some particles that replace Pt as counter electrodes to the FTO glass substrate. It is well known that the surface area theoretical value of graphene reaches 2600 m^2/g,[40] such high surface area leads to easily capturing of electrons from redox couples (I^-/ I^{3-}) in the electrolyte, and thus the redox couples are easily reduced. This process will benefit electron transmission across the CE/ substrate interface. On the other hand, the high surface area of rGO is beneficial for the enhancement of visible light absorption. Figure 10 shows the optical property of six Bi_2S_3-based materials, the absorption was increased as increasing the rGO content. The introduction of rGO in the system was limited to the surface of Bi_2S_3 structures. The electrons generated near an electrode surface have a higher potential for electron loss by recombination due to a longer transport time prior to collection at the FTO substrate. Therefore, this surface limited mixing can improve the overall electron transport in an effective manner and then enhance the energy conversion efficiency.[41] As shown in table 1, the energy conversion efficiency was increased as increasing the rGO content. However, excessive addition of rGO made the energy conversion efficiency decline. It was attributed to the amount of light was absorption by the rGO, rather decreased the light absorption by dye molecules, which brings on impaired light harvesting efficiency decreasing light reflected from CE to photoanode.[42] Thus, suitable rGO content will ensure high energy conversion efficiency.

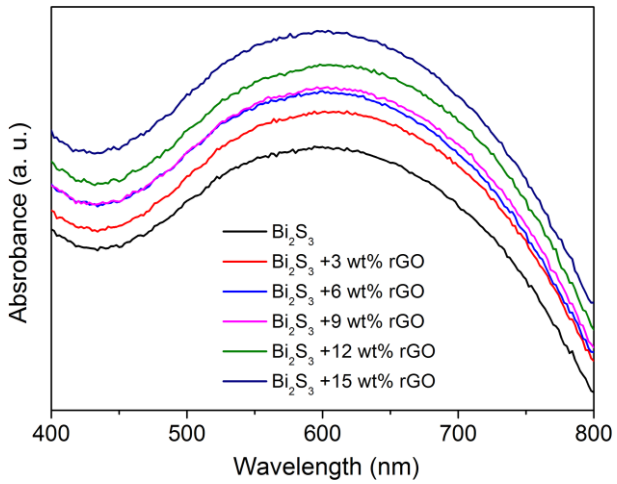

Figure 10. UV-Vis spectra of Bi_2S_3 nanorods with various wt % of rGO.

Compared with reported 3D Bi_2S_3 microspheres comprised of nanorods on graphene, mesoporous Bi_2S_3 nanorods with graphene assist exhibit much higher photoelectric conversion efficiency. Considering the high performance and more concise synthesis process of Bi_2S_3+ 9 wt% rGO CE, Bi_2S_3 nanorods with appropriate amount of graphene assist expected to have great potential in replacing the expensive Pt in DSCs as a promising low-cost and effective CE catalyst. In recent years, many chemists have made great contributions to photoanode in DSCs, and a large number of excellent performance photoanode materials had been reported.[43-45] For us, we are always committed to the study of CE materials, and we will attempt to improve our fabrication process to achieve higher performance DSCs based on Bi_2S_3 in the future.

Conclusion

In summary, we successfully synthesized mesoporous Bi_2S_3 nanorods through a facile strategy. These Bi_2S_3 products showed potential applications for DSCs, which could be used as an efficient alternative for Pt. With the simple physical mixture of reduced graphene oxides, Bi_2S_3-based CEs exhibited excellent electrochemical catalytic activity for catalyzing the reduction of triiodide. This is the first time to investigate the photovoltaic properties of Bi_2S_3 nanorods mixing with graphene among different amount. Our method is robust, low-cost, simple, and efficient. It is also expected

that this series of mesoporous Bi_2S_3 nanorods mixing with graphene materials may find other applications such as optoelectrical devices and photocatalysis.

Acknowledgements

This work was supported by the National Science Foundation of China (No. 21271108), the Ministry of Science and Technology (Grant 2014CB932001), 2011 Science Foundation of Tianjin (No. 11JCZDJC24800), and China–U.S. Center for Environmental Remediation and Sustainable Development.

References

1 M. Grätzel, *Nature*, 2001, **414**, 338–344.

2 B. O'Regan and M. Grätzel, *Nature*, 1991, **353**, 737–740.

3 G. Calogero, P. Calandra, A. Irrera, A. Sinopoli, I. Citro and G. Di Marco, *Energy Environ. Sci.*, 2011, **4**, 1838–1844.

4 M. X. Wu, Y. D. Wang, X. Lin, W. Guo, K. Z. Wu, Y. N. Lin, H. Y. Guo and T. L. Ma, *J. Mater. Chem. A*, 2013, **1**, 9672–9679.

5 R. Bashyam and P. Zelenay, *Nature*, 2006, **443**, 63–66.

6 W. J. Wang, X. Pan, W. Q. Liu, B. Zhang, H. W. Chen, X. Q. Fang, J. X. Yao and S. Y. Dai, *Chem. Commun.*, 2014, **50**, 2618–2620.

7 H. M. Chuang, C. T. Li, M. H. Yeh. C. P. Lee, R. Vittal and K. C. Ho, *J. Mater. Chem. A*, 2014, **2**, 5816–5824.

8 Y. C. Wang, D. Y. Wang, Y. T. Jiang, H. A. Chen, C. C. Chen, K. C. Ho, H. L. Chou and C. W. Chen, *Angew. Chem. Int. Ed.*, 2013, **52**, 6694–6698.

9 X. Chen, Z. M. Bai, X. Q. Yan, H. G. Yuan, G. J. Zhang, P. Lin, Z. Zhang, Y. C. Liu and Y. Zhang, *Nanoscale*, 2014, **6**, 4691–4697.

10 X. J. Zheng, J. Deng, N. Wang, D. H. Deng, W. H. Zhang, X. H. Bao and C. Li, *Angew. Chem.*, 2014, **126**, 7143–7147.

11 M. J. Ju, J. C. Kim, H-J. Choi, I. T. Choi, S. G. Kim, K. Lim, J. Ko, J-J. Lee, I-Y. Jeon, J-B. Baek and H. K. Kim, *ACS Nano*, 2013, **7**, 5243–5250.

12 L. Cademartiri, R. Malakooti, P. G. O. Brien, A. Migliori, S. Petrov, N. P. Kherani and G. A. Ozin, *Angew. Chem., Int. Ed.*, 2008, **47**, 3814–3817.

13 H. H. Li, J. Yang, J. Y. Zhang and M. Zhou, *RSC Adv.*, 2012, **2**, 6258–6261.

14 Y. Tian, C. F. Guo, S. M. Guo, T. F. Yu and Q. Liu, *Nano Res*., 2014, **7**, 953–962.

15 Y. Zhao, D. L. Gao, J. F. Ni, L. J. Gao, J. Yang and Y. Li, *Nano Res*., 2014, **7**, 765–773.

16 G. Li, X. S. Chen and G. D. Gao, *Nanoscale*, 2014, **6**, 3283–3288.

17 L. M. Peter, K. G. U. Wijayantha, D. J. Riley and J. P. Waggett, *J. Phys. Chem. B*, 2003, **107**, 8378–8381.

18 H. J. Zhang, L. T. Yang, Z. Liu, M. Ge, Z. Zhou, W. Chen, Q. Z. Li and L. Liu, *J. Mater. Chem.*, 2012, **22**, 18572–18577.

19 N. J. Bell, H. N. Yun, A. J. Du, H. Coster, S. C. Smith and R. Amal, *J. Phys. Chem. C*, 2011, **115**, 6004–6009.

20 N. Yang, J. Zhai, D. Wang, Y. Chen and L. Jiang, *ACS Nano*, 2010, **4**, 887–894.

21 M. M. Zhen, L. W. Su, Z. H. Yuan, L. Liu, Z. Zhou, *RSC Adv.*, 2013, **3**, 13696–13701.

22 R. Bajpai, S. Roy, N. Kulshrestha, J. Rafiee, N. Koratkar and D. S. Misra, *Nanoscale*, 2012, **4**, 926–930.

23 J. H. Lehman, M. Terrones, E. Mansfield, K. E. Hurst and V. Meunier, *Carbon*, 2011, **49**, 2581–2602.

24 S. Q. Guo, X. Zhang, Z. Zhou, G. D. Gao and L. Liu, *J. Mater. Chem. A*, 2014, **2**, 9236–9243.

25 C. S. Guo, M. Ge, L. Liu, G. D. Gao, Y. C. Feng and Y. Q. Wang, *Environ. Sci. Technol.*, 2010, **44**, 419–425.

26 Y. Zhang, Z. B. Xie and J. Wang, *ACS Appl. Mater. Interfaces*, 2009, **1**, 2789–2795.

27 L. Andrade, S. M. Zakeeruddin, M. K. Nazeeruddin, H. A. Ribeiro, A. Mendes and M. Gratzel, *ChemPhysChem*, 2009, **10**, 1117–1124.

28 A. Zaban, J. Zhang, Y. Diamant, O. Melemed and J. Bisquert, *J. Phys. Chem. B*, 2003, **107**, 6022–6025.

29 M. Toivola, L. Peltokorpi, J. Halme and P. Lund, *Sol. Energy Mater. Sol. Cells*, 2007, **91**, 1733−1742.

30 A. I. Popov and D. H. Geske, *J. Am. Chem. Soc.*, 1958, **80**, 1340–1352.

31 Z. Huang, X. Z. Liu, K. X. Li, D. M. Li, Y. H. Luo, H. Li, W. B. Song, L. Q. Chen and Q. B. Meng, *Electrochem. Commun.*, 2007, **9**, 596–598.

32 Y. Bai, X. Zong, H. Yu, Z. G. Chen and L. Z. Wang, *Chem. Eur. J.*, 2014, **20**, 1–8.

33 J. Chen, K. Li, Y. Luo, X. Guo, D. Li, M. Deng, S. Huang and Q. Meng, *Carbon*, 2009, **47**, 2704–2708.

34 F. Fabregat-Santiago, J. Bisquert, E. Palomares, L. Otero, D. Kuang, S. M. Zakeeruddin and M. Grätzel, *J. Phys. Chem. C*, 2007, **111**, 6550–6560.

35 X. Chen, Y. Hou, B. Zhang, X. H. Yang and H. G. Yang, *Chem. Commun.*, 2013, **49**, 5793–5795.

36 M. X. Wu, X. Lin, T. H. Wang, J. S. Qiu and T. L. Ma, *Energy Environ. Sci.*, 2011, **4**, 2308–2315.

37 M. X. Wu, X. Lin, A. Hagfeldt and T. L. Ma, *Angew. Chem., Int. Ed.*, 2011, **50**, 3520–3524.

38 S. M. Zakeeruddin and M. Grätzel, *Adv. Funct. Mater.*, 2009, **19**, 2187–2202.

39 M. K. Wang, A. M. Anghel, B. Marsan, N. C. Ha, N. Pootrakulchote, S. M. Zakeeruddin and M. Grätzel, *J. Am. Chem. Soc.*, 2009, **131**, 15976–15977.

40 S. Stankovich, D. A. Dikin, G. H. B. Dommett, K. M. Kohlhaas, E. J. Zimney, E. A. Stach, R. D. Piner, S. B. T. Nguyen and R. S. Ruoff, *Nature*, 2006, **442**, 282–286.

41 H. N. Kim, H. Yoo and J. H. Moon, *Nanoscale*, 2013, **5**, 4200–4204.

42 M. Y. Liu, G. Li and X. S. Chen, *ACS Appl. Mater. Interfaces*, 2014, **6**, 2604–2610.

43 X. Yin, B. Wang, M. He and T. He, *Nano Res.*, 2012, **5**, 1–10.

44 J. X. Shi, Y. X. Liu, Q. Peng and Y. D. Li, *Nano Res.*, 2013, **6**, 441–448.

45 H. M. Zhang, H. Yu, Y. H. Han, P. R. Liu, S. Q. Zhang, P. Wang, Y. B. Cheng and H. J. Zhang, *Nano Res.*, 2011, **4**, 938–947.